INTERNATIONAL JOURNAL FOR NUMERICAL METHODS IN ENGINEERING
Int. J. Numer. Meth. Engng 2000; **00**:1–6 *Prepared using* nmeauth.cls *[Version: 2002/09/18 v2.02]*

A Discontinuous Enrichment Method for Three-Dimensional Multiscale Harmonic Wave Propagation Problems in Multi-Fluid and Fluid-Solid Media

Paolo Massimi*, Radek Tezaur and Charbel Farhat

Department of Mechanical Engineering and Institute for Computational and Mathematical Engineering Stanford University, Mail Code 3035, Stanford, CA 94305, U.S.A.

SUMMARY

An evanescent wave occurs when a propagating incident wave impinges on an interface between two fluid, solid, or fluid-solid media at a subcritical angle. Mathematical properties of such a wave makes it difficult to capture with standard finite element discretization schemes. For this reason, the discontinuous enrichment method (DEM) developed in [1, 2, 3, 4, 5, 6, 7, 8] is extended here to the solution of a class of three-dimensional evanescent wave problems in the frequency domain. To this effect, new DEM elements for three-dimensional elastodynamic problems are first proposed. Then, these and other DEM elements previously developed for the efficient solution of the Helmholtz problem are further enriched with free-space solutions of model evanescent wave problems, in order to achieve high accuracy at practical mesh resolution for fluid-fluid and fluid-solid applications. The performance of the extended DEM elements is reported to be better than that of its basic Helmholtz and Navier counterparts, and superior to that achieved by the classical high-order polynomial finite element method. Copyright © 2000 John Wiley & Sons, Ltd.

KEY WORDS: discontinuous Galerkin, enrichment, evanescent waves, fluid-structure, Helmholtz, Lagrange multipliers, medium frequency, multiscale, wave propagation

1. INTRODUCTION

Wave propagation continues to attract considerable scientific interest because of its numerous applications. It also raises numerous challenges with respect to numerical modeling. One of the principal difficulties consists in capturing the waves numerically over large distances. This paper concentrates on another aspect of wave propagation which occurs, for example, in layered media. When an incident wave encounters a material interface, one of two scenarios occurs: either some part of its energy is reflected back and another part gives rise to a refracted wave

*Correspondence to: Paolo Massimi, Department of Mechanical Engineering and Institute for Computational and Mathematical Engineering, Mail Code 3035, Stanford, CA 94305, U.S.A.
Email: cfarhat@stanford.edu

Contract/grant sponsor: Office of Naval Research; contract/grant number: N00014-05-1-0204-1

Received 20 December 2007
Revised

that penetrates and propagates into the second material (Figure 1-left), or all of the energy is reflected back. The latter scenario is called a total reflection and occurs at angles below the so-called critical angle. Even though no energy is transmitted through the interface, a disturbance is still produced at the other side of it. This disturbance, which can be viewed as a small-scale feature of wave propagation, is called an *evanescent wave* (Figure 1-right). Compared to the large-scale refracted wave, the evanescent wave is small-scale and decays rapidly away from the interface. It can be shown that the decay in the direction perpendicular to the interface is exponential and thus can lead to a very high gradient of the solution.

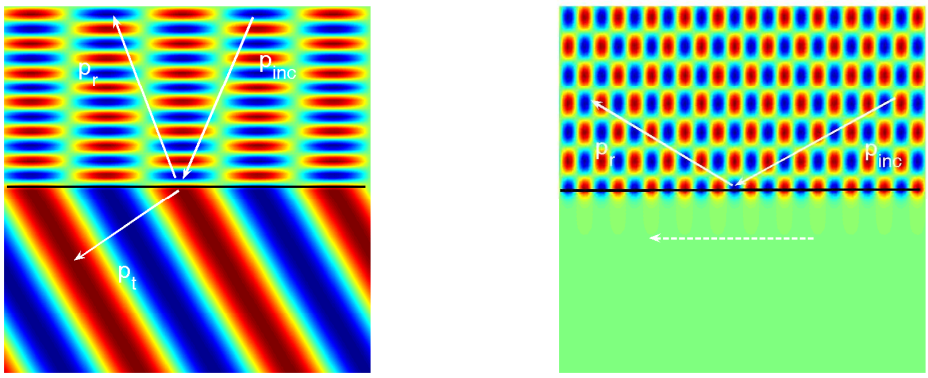

Figure 1. Example of a refracted wave created by an incident wave at 80° in a given plane (left), and evanescent wave created by an incident wave at 30° in that plane (right). The upper-half of the domain is air, the lower-half is water. The critical angle is $\theta_{\text{cr}} = 77.16°$.

To capture the small scale of the evanescent waves, it is possible to use graded meshes. This generates however a large number of degrees of freedom and potentially prohibitive costs. Another approach is to enrich the approximation spaces with functions that capture well the characteristics of the solution. This is the idea adopted in this paper. It has been used by a number of finite element techniques, both in the context of wave propagation and other multiscale problems. These include the generalized finite element method (GFEM) [20, 21, 22, 23], the extended finite element method (XFEM) [24, 25, 26, 27], the *hp* cloud method [28, 29], the least squares method [30], the weak element method [31], the ultra-weak method [31], the variational theory of complex rays [32], and the discontinuous enrichment method (DEM).

The discontinuous enrichment method, which is the focus of this paper, is a hybrid discontinuous Galerkin method with Lagrange multipliers. It was originally developed [1] for the solution of multiscale boundary value problems with sharp gradients and oscillations. In this method, the standard finite element polynomial field, which represents the coarse scale of the solution, is enriched within each element by free-space solutions of the homogeneous partial differential equation to be solved. Since these solutions may be discontinuous across the element interfaces, Lagrange multipliers are introduced there to enforce a weak continuity of the solution. For some problems, the polynomial part of the approximation can be dropped, thereby transforming DEM into a non-standard discontinuous Galerkin method (DGM). The method

has matured since the initial development of two-dimensional elements for the Helmholtz equation on uniform meshes [2]. High-order quadrilateral DGM elements have been developed, coupled with a suitable absorbing boundary condition for scattering problems and shown to outperform classical polynomial approximations [5, 4]. The method has been extended to the three-dimensional Helmholtz equation [7] and to two-dimensional elastodynamic harmonic problems [6]. A preliminary study of DEM in the context of two-dimensional evanescent waves has also been reported in [8].

The main objectives of this paper are to extend the concepts previously studied in two dimensions to three dimensions and demonstrate that they can be successfully applied to the efficient solution of layered, multiscale, fluid-fluid and fluid-solid problems. To this effect, this paper is organized as follows. First, the mathematical formulation of DEM for a coupled three-dimensional fluid-solid problem is presented in Section 2. After reviewing some key aspects of DEM and the corresponding three-dimensional Helmholtz elements, new three-dimensional elastodynamic (Navier) DEM elements are proposed in Section 3. Then, new DEM elements with evanescent waves are constructed based on analytical solutions near generic fluid/fluid and fluid/solid interfaces. In Section 4, the performance of these new elements is evaluated for several benchmark problems. Finally, conclusions are presented in Section 5.

2. MATHEMATICAL FORMULATION OF ACOUSTIC PROBLEMS IN COMPRESSIBLE FLUIDS AND ELASTIC SOLIDS

A mathematical framework for acoustic fluid-solid interaction problems is presented here. The formulation addresses the general heterogeneous problem and can be easily reduced to single- or multi-layered problems for fluid or solid media. The associated hybrid variational formulation is also addressed in order to establish the natural mathematical framework for the DEM method.

The wave propagation problem is formulated in a domain $\Omega = \Omega_f \bigcup \Omega_s$, where Ω_f and Ω_s are fluid and solid subdomains, respectively. For simplicity, the solid material is assumed to be isotropic and linearly elastic. A time-harmonic elastic wave propagation is governed by Navier's equations [9]

$$\mu_L \Delta \underline{u} + (\lambda_L + \mu_L)\nabla(\nabla \cdot \underline{u}) + \rho_s \omega^2 \underline{u} = -\underline{f}(\underline{x}), \qquad \text{in } \Omega_s. \tag{1}$$

Here, ρ_s is the density of the elastic material, λ_L and μ_L are its Lamé constants, ω is the circular frequency, $\underline{f}$ is the body force, and $\underline{u} \equiv \underline{u}(\underline{x})$ is the displacement field in Ω_s.

Let

$$M = \begin{bmatrix} \lambda_L + 2\mu_L & \lambda_L & \lambda_L & 0 & 0 & 0 \\ \lambda_L & \lambda_L + 2\mu_L & \lambda_L & 0 & 0 & 0 \\ \lambda_L & \lambda_L & \lambda_L + 2\mu_L & 0 & 0 & 0 \\ 0 & 0 & 0 & \mu_L & 0 & 0 \\ 0 & 0 & 0 & 0 & \mu_L & 0 \\ 0 & 0 & 0 & 0 & 0 & \mu_L \end{bmatrix} \quad \text{and} \quad D = \begin{bmatrix} \frac{\partial}{\partial x} & 0 & 0 \\ 0 & \frac{\partial}{\partial y} & 0 \\ 0 & 0 & \frac{\partial}{\partial z} \\ \frac{\partial}{\partial y} & \frac{\partial}{\partial x} & 0 \\ 0 & \frac{\partial}{\partial z} & \frac{\partial}{\partial y} \\ \frac{\partial}{\partial z} & 0 & \frac{\partial}{\partial x} \end{bmatrix}. \tag{2}$$

Then, Navier's equations (1) can also be written concisely as

$$D^T M D\underline{u} + \rho_s \omega^2 \underline{u} = -\underline{f}, \qquad \text{in } \Omega_s, \tag{3}$$

where the superscript T designates the transpose operation. The wave propagation in the fluid subdomain Ω_f is governed by the Helmholtz equation

$$\Delta p + k_f^2 p = 0, \qquad \text{in } \Omega_f, \tag{4}$$

where $p \equiv p(\underline{x})$ is the pressure field,

$$k_f = \frac{\omega}{c_f} \tag{5}$$

is the wave number in the fluid subdomain Ω_f, and c_f is the speed of sound in Ω_f. Equilibrium and compatibility at the interface $\Gamma_0 = \partial\Omega_f \bigcap \partial\Omega_s$ yield the following transmission conditions

$$\rho_f \omega^2 \underline{u} \cdot \underline{n} = \frac{\partial p}{\partial \underline{n}}, \qquad \text{on } \Gamma_0, \tag{6}$$

$$\underline{\underline{\sigma}}(\underline{u})\underline{n} \cdot \underline{n} + p = 0, \qquad \text{on } \Gamma_0, \tag{7}$$

where ρ_f is the density of the fluid, $\underline{n}$ is the normal direction on the fluid/solid interface Γ_0 from the solid side, and $\underline{\underline{\sigma}}$ is the stress tensor. Without any loss of generality, the following boundary conditions are considered

$$\underline{\underline{\sigma}}(\underline{u})\underline{n} = \underline{g}_s, \qquad \text{on } \Gamma_s, \tag{8}$$

$$\frac{\partial p}{\partial \underline{n}} - ik_f p = g_f, \qquad \text{on } \Gamma_f, \tag{9}$$

where $\Gamma_f = \partial\Omega_f \backslash \Gamma_0$, $\Gamma_s = \partial\Omega_s \backslash \Gamma_0$, g_f is the excitation on Γ_f, and $\underline{g}_s$ is the specified traction on Γ_s. Let Ω_f and Ω_s be partitioned into n_f and n_s elements, respectively, i.e.

$$\overline{\Omega}_f = \bigcup_{j=1}^{n_f} \overline{\tau}_j^f, \qquad \tau_j^f \bigcap \tau_l^f = \emptyset \quad \text{if } j \neq l, \quad j, l = 1, 2, ..., n_f, \tag{10}$$

$$\overline{\Omega}_s = \bigcup_{j=1}^{n_s} \overline{\tau}_j^s, \qquad \tau_j^s \bigcap \tau_l^s = \emptyset \quad \text{if } j \neq l, \quad j,l = 1,2,...,n_s. \tag{11}$$

Let $\Delta_h^f = \{\tau_j^f\}_{j=1}^{n_f}$ and $\Delta_h^s = \{\tau_j^s\}_{j=1}^{n_s}$ be the set of all elements in Ω_f and Ω_s, respectively. Furthermore, let $\mathcal{U}^f$, Λ^f, $\mathcal{U}^s$ and Λ^s denote the following spaces

$$\mathcal{U}^f = \prod_{\tau \in \Delta_h^f} H^1(\tau), \qquad \Lambda^f = \prod_{\tau_j \in \Delta_h^f} \prod_{\tau_l \in \Delta_h^f, j<l} H^{-1/2}(\partial\tau_j \bigcap \partial\tau_l), \tag{12}$$

$$\mathcal{U}^s = \prod_{\tau \in \Delta_h^s} \big(H^1(\tau)\big)^3, \tag{13}$$

$$\Lambda^s = \Big\{ \underline{\lambda} \in \prod_{\tau_j \in \Delta_h^s} \prod_{\substack{\tau_l \in \Delta_h^s \\ j<l}} \big(H^{-1/2}(\partial\tau_j \bigcap \partial\tau_l)\big)^3 \quad \text{such that} \tag{14}$$

$$\forall \underline{\lambda}|_{\partial\tau_j \bigcap \partial\tau_l} \; \exists \underline{\underline{\sigma}} \in H(div;\Omega_s) \;\; s.t. \;\; \underline{\underline{\sigma}} \cdot \underline{n} = \underline{\lambda} \;\; \text{on} \;\; \partial\tau_j \bigcap \partial\tau_l \Big\},$$

where H^1 and $H^{-1/2}$ are the usual Sobolev spaces [33], and

$$H(div;\Omega_s) = \Big\{ \underline{\underline{\sigma}} \in \big(L_2(\Omega_s)\big)^{3\times 3} : \sigma_{jl} = \sigma_{lj}, 1 \leq j,l \leq 3, \; div\underline{\underline{\sigma}} = \Big(\sum_{l=1}^{3} \frac{\partial \sigma_{jl}}{\partial x_l} \Big)_{1\leq j\leq 3} \in \big(L_2(\Omega_s)\big)^3 \Big\}. \tag{15}$$

Then, the hybrid weak form of the boundary value problem (3-9) can be written as follows *Find* $(p,\lambda^f) \in \mathcal{U}^f \times \Lambda^f$ *and* $(\underline{u},\underline{\lambda}^s) \in \mathcal{U}^s \times \Lambda^s$ *such that*

$$a_f(p,q) + b_f(\lambda^f,q) + \omega^2 c(\underline{u},q) = r_f(q), \quad \forall q \in \mathcal{U}^f, \tag{16}$$

$$a_s(\underline{u},\underline{v}) + b_s(\underline{\lambda}^s,\underline{v}) + c(\underline{v},p) = r_s(\underline{v}), \quad \forall \underline{v} \in \mathcal{U}^s, \tag{17}$$

$$b_f(\mu^f,p) = 0, \qquad \forall \mu^f \in \Lambda^f, \tag{18}$$

$$b_s(\underline{\mu}^s,\underline{u}) = 0, \qquad \forall \underline{\mu}^s \in \Lambda^s, \tag{19}$$

where $a_f(\cdot,\cdot)$ is the bilinear form defined on $\mathcal{U}^f \times \mathcal{U}^f$ as

$$a_f(p,q) = \frac{1}{\rho_f} \sum_{\tau \in \Delta_h^f} \int_\tau (\nabla p \cdot \nabla q - k_f^2 pq) dx - \frac{1}{\rho_f} \int_{\Gamma_f} ik_f pq ds, \tag{20}$$

$b_f(\cdot,\cdot)$ is defined on $\Lambda^f \times \mathcal{U}^f$ as

$$b_f(\lambda^f,p) = \frac{1}{\rho_f} \sum_{\tau_j \in \Delta_h^f} \sum_{\substack{\tau_l \in \Delta_h^f \\ j<l}} \int_{\partial\tau_j \cap \partial\tau_l} \lambda^f (p|_{\tau_j} - p|_{\tau_l}) ds, \tag{21}$$

$a_s(\cdot,\cdot)$ and $b_s(\cdot,\cdot)$ are defined on $\mathcal{U}^s \times \mathcal{U}^s$ and $\Lambda^s \times \mathcal{U}^s$, respectively, as

$$a_s(\underline{u},\underline{v}) = \sum_{\tau \in \Delta_h^s} \int_\tau \Big(D\underline{v}\Big)^T M\Big(D\underline{u}\Big) \, dx - \rho_s \omega^2 \sum_{\tau \in \Delta_h^s} \int_\tau \underline{u} \cdot \underline{v} \, dx, \tag{22}$$

$$b_s(\underline{\lambda},\underline{v}) = \sum_{\tau_j\in\Delta_h^s}\sum_{\substack{\tau_l\in\Delta_h^s\\ j<l}}\int_{\partial\tau_j\cap\partial\tau_l}\underline{\lambda}\cdot(\underline{v}|_{\tau_j}-\underline{v}|_{\tau_l})\,ds, \tag{23}$$

$c(\cdot,\cdot)$ is the coupling term defined on $\mathcal{U}^s\times\mathcal{U}^f$ as

$$c(\underline{u},p) = \int_{\Gamma_0} p(\underline{u}\cdot\underline{n})ds, \tag{24}$$

and the linear forms $r_f(\cdot)$ and $r_s(\cdot)$ are defined on $\mathcal{U}^f$ and $\mathcal{U}^s$, respectively, as

$$r_f(q) = \frac{1}{\rho_f}\int_{\Gamma_f} g_f q ds, \tag{25}$$

$$r_s(\underline{v}) = \int_{\Omega_s}\underline{f}\cdot\underline{v}\,dxdy + \int_{\Gamma_s}\underline{g}_s\cdot\underline{v}\,ds. \tag{26}$$

Let $\mathcal{U}_h^f$, Λ_h^f, $\mathcal{U}_h^s$ and Λ_h^s be finite dimensional spaces satisfying

$$\mathcal{U}_h^f\subset\mathcal{U}^f,\quad \Lambda_h^f\subset\Lambda^f,\quad \mathcal{U}_h^s\subset\mathcal{U}^s\quad\text{and}\quad\Lambda_h^s\subset\Lambda^s. \tag{27}$$

Then, the discretization of the hybrid variational formulation described above is obtained in a standard way by replacing the continuous spaces in (16-19) by their discrete subspaces (27). The problem(16-19) describes a general setting for a multi–phase heterogeneous problem for acoustic wave propagation in solid and fluid media. If the coupling term c in equations (16) and (17) is dropped, the system (16) and (18) describes the propagation of acoustic waves in a fluid medium, and the system (17) and (19) describes the elastodynamic problem associated with the propagation of an acoustic wave in an elastic medium.

3. DEM METHODOLOGY AND THREE–DIMENSIONAL DEM ELEMENTS

In general, DEM [1, 2, 3, 4, 5, 6, 7] seeks an approximate solution of its hybrid variational problem in the form of a locally enriched polynomial. For example, in the case of Navier's elastodynamic equations (1), it approximates the solution $\underline{u}$ by

$$\underline{u}_h = \underline{u}_h^P + \underline{u}_h^E, \tag{28}$$

where $\underline{u}_h^P\in\mathcal{U}_h^P$ is based on the classical (low-order) finite element polynomials which are suitable for representing the large scales of the solution [3], and $\underline{u}_h^E\in\mathcal{U}_h^E$ denotes the enrichment that should be suitable for representing its small scales [3], so that

$$\mathcal{U}_h = \mathcal{U}_h^P\oplus\mathcal{U}_h^E. \tag{29}$$

Note that in the above decomposition, the superscript s has been dropped from $\mathcal{U}_h$ to indicate its suitability for fluid problems too. Usually, the enrichment field is constructed from the free-space solutions of the homogeneous part of the governing partial differential equations that are not contained in $\mathcal{U}_h^P$. For a large class of Helmholtz problems such as those arising in acoustic scattering, the exact solution can be well represented using only the free-space solutions of the governing partial differential equation. For such problems, DEM drops the polynomial

field from the numerical approximation, in which case the enriched elements are labeled DGM (Discontinuous Galerkin) elements instead of DEM elements. On the other hand, one can find in the solution of elastodynamic problems non oscillatory or slowly oscillatory components in space due to a specific type of loading. For this reason, DEM can maintain the polynomial field in the numerical approximation when applied to the solution of some elastodynamic problems, and the enriched elements are labeled in this case DEM elements.

As with every hybrid method, special attention needs to be paid to the choice of the Lagrange multipliers in order to satisfy the *inf–sup* condition. To this effect, the following "limitation" criterion, which was justified in [2, 4, 5], is adopted here

$$n^{\lambda} \leq \frac{n^{E}}{2}, \tag{30}$$

where n^{λ} denotes the total number of Lagrange multiplier degrees of freedom per face, and n^{E} denotes the total number of enrichment functions per element — that is, the dimension of $\mathcal{U}_h^E$. The discontinuous enrichment finite element concept can be viewed as a p-type (polynomial) finite element method in the sense that increasing the number of enrichment functions is akin to increasing the degree of a polynomial approximation. Both approaches are limited by numerical conditioning and computational complexity issues. In practical DEM/DGM computations, the enrichment degrees of freedom can be condensed out at the local (element) level. Hence, the overall computational complexity of a DEM/DGM discretization is determined mostly by the number of Lagrange multiplier and polynomial degrees of freedom.

Next, a family of three-dimensional elements for Helmholtz problems with an increasing number of plane wave and Lagrange multiplier degrees of freedom previously developed in [7] is reviewed for the sake of completeness.

3.1. DGM elements for three-dimensional Helmholtz problems

In this case, the space $\mathcal{U}_h^{f,E}$ is chosen as a superposition of planar waves. In the general case of n^E planar waves described by unitary directions of propagation $\underline{\Theta}_p$, $p = 1, \ldots, n^E$, this discontinuous space may be written as

$$\begin{aligned}\mathcal{U}_h^{f,E} = \{p_h^E \in L^2(\Omega_f) : p_h^E\big|_{\tau} = \sum_{p=1}^{n^E} p_p e^{ik_f \underline{\Theta}_p^T \cdot \underline{x}}, \underline{x} \in \mathbb{R}^3, p_p \in \mathbb{C},\\ \underline{\Theta}_p \in \mathbb{R}^3, ||\underline{\Theta}_p|| = 1, p = 1, \ldots, n^E, \underline{\Theta}_p \neq \underline{\Theta}_q \text{ if } \quad p \neq q\}.\end{aligned} \tag{31}$$

The complex coefficients p_p are the primal degrees of freedom in the element τ.

The other critical aspect of the DEM method is the choice of the Lagrange multipliers on the element interfaces. It can be shown [2] that the exact solution p and the Lagrange multiplier λ of the hybrid formulation for the Helmholtz problem are related on the interface between elements τ and τ' by

$$\lambda = \frac{\partial p}{\partial \underline{n}}, \qquad \text{on } \partial\tau \bigcap \partial\tau'. \tag{32}$$

This suggests choosing λ_h as a good approximation of $\dfrac{\partial p}{\partial \underline{n}}$ and leads to the following space of

approximation for the Lagrange multiplier field

$$\Lambda_h^f = \Big\{ \lambda_h \in \Lambda^f : \lambda_h\big|_{\partial\tau \bigcap \partial\tau'}(\underline{t}) = \sum_{p=1}^{n^\lambda} \lambda_p e^{ik_f c_p \phi_p^T \underline{t}}, \quad \lambda_p \in \mathbb{C},\ p = 1, \ldots, n_\lambda,$$
$$\phi_p \text{ are given unitary directions in } \mathbb{R}^2, \quad c_p \in \mathbb{R} \text{ are given coefficients,}$$
$$\underline{t} \in \mathbb{R}^2 \text{ are local orthogonal coordinates on the face } \quad \Gamma^{\tau,\tau'} : \underline{x} = \underline{x}(\underline{t}) \Big\} \tag{33}$$

where τ and τ' are two neighboring elements and n^λ determines the dimension of Λ_h^f on each face. Details about the choice of the directions of the enrichment field and those of the corresponding Lagrange multipliers and various implementation details can be found in [7].

Figure 2 shows the directions of the plane waves included in the enrichment field and corresponding Lagrange multipliers for two elements that will play a role later in this paper. The first one, DGM element H–26–4 employs 26 waves in the enrichment field and four Lagrange multipliers per face. It has a computational complexity that is similar to that of the classical quadratic element Q_2 but a significantly better performance. The second DGM element for Helmholtz applications, H–56–8, utilizes 56 planar waves and eight Lagrange multipliers per face. It features a computational complexity per element and a convergence rate that are similar to those of the classical cubic element Q_3. However, it delivers a significantly better performance. For example, it was shown in [7] that in the medium frequency regime, both DGM elements H–26–4 and H–56–8 reduce by one to two orders of magnitude the CPU time required by the standard p-type (polynomial) finite elements with comparable computational complexities and convergence rates, when applied to the solution of three-dimensional wave guide and acoustic scattering problems.

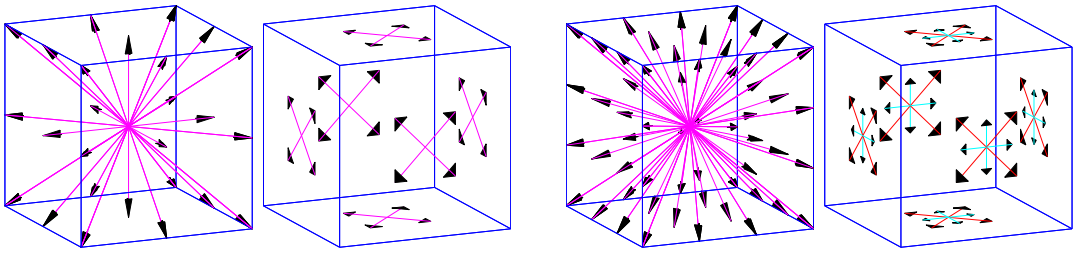

(a) H–26–4 (b) H–56–8

Figure 2. Directions of the enrichment field inside the element (solution) and on its faces (Lagrange multipliers) for elements H–26–4 (a) and H–56–8 (b).

3.2. DEM elements for three-dimensional elastodynamic problems

The concepts underlying the construction of DEM elements for the solution of two-dimensional elastodynamic problems were discussed in [6]. Here, these concepts are extended to three dimensions, and a new family of DEM elements for the solution of the Navier equations is proposed. For simplicity, the case of a homogeneous isotropic material is considered.

In general, free-space solutions of the homogeneous part of the partial differential equation of interest are used by DEM to construct an enrichment field for the approximation. In this case, three linearly independent solutions of Eq. (3) in the form of planar waves can be found for any direction of propagation: a pressure (longitudinal) wave, and two shear (transversal) waves. Hence, the enrichment space $\mathcal{U}_h^{s,E}$ is chosen as

$$\mathcal{U}_h^{s,E} = \{\underline{u}_h^E \in (L^2(\Omega_s))^3 : \underline{u}_h^E\big|_\tau = \sum_{q=1}^{n^E} \underline{u}_{P_q}^E \underline{\Theta}_q e^{ik_p \underline{\Theta}_q \cdot \underline{x}} + \sum_{q=1}^{n^E} \underline{u}_{1,S_q}^E \underline{\Theta}_q^\perp e^{ik_s \underline{\Theta}_q \cdot \underline{x}} + \sum_{q=1}^{n^E} \underline{u}_{2,S_q}^E \underline{\Theta}_q^{\perp\perp} e^{ik_s \underline{\Theta}_q \cdot \underline{x}}\} \tag{34}$$

where $\underline{u}_{P_q}$, $\underline{u}_{1,S_q}$ and $\underline{u}_{2,S_q}$ are the q–th pressure and shear amplitude vectors, and $\underline{\Theta}_q$ is the q–th direction of propagation of the elastic pressure and shear waves. The elastic wave numbers k_p and k_s are given by

$$k_p = \omega\sqrt{\frac{\rho}{\lambda_L + 2\mu_L}} \quad \text{and} \quad \mathrm{k_s} = \omega\sqrt{\frac{\rho}{\mu_L}}. \tag{35}$$

As shown in [6], the exact solution u of the hybrid problem and the Lagrange multiplier $\underline{\lambda}$ are related on the element interfaces by

$$\underline{\lambda} = \underline{\underline{\sigma}}(\underline{u})\underline{n}, \qquad \text{on } \partial\tau \bigcap \partial\tau'. \tag{36}$$

This indicates that the Lagrange multipliers should be chosen as approximations of the tractions of the solution. Here, the traction of another carefully set of pressure and shear waves is used,

$$\Lambda_h^s = \left\{\underline{\lambda}_h \in \Lambda^s : \underline{\lambda}_h\big|_{\partial\tau \bigcap \partial\tau'}\right\} = \sum_{j=1}^{n^{\lambda_p}} \eta_j^p \underline{\underline{\sigma}}(\underline{\Theta}_j^p e^{ik_p \underline{\Theta}_j^p \cdot \underline{x}}) + \sum_{j=1}^{n^{\lambda_s}} \eta_j^s \underline{\underline{\sigma}}(\underline{\Theta}_j^{s\perp} e^{ik_s \underline{\Theta}_j^s \cdot \underline{x}})\Big\} \tag{37}$$

where n^{λ_p} and n^{λ_s} denote the number of Lagrange multipliers arising from pressure and shear waves on each face of the element respectively, and η_j^p and η_j^s are the dual degrees of freedom on the edge $\partial\tau \bigcap \partial\tau'$. To compute the tractions, the following relationships can be conveniently used for pressure waves

$$\underline{\underline{\sigma}}(\underline{\Theta}_q e^{ik_p \underline{\Theta}_q \cdot \underline{x}})\underline{n} = ik_p e^{ik_p \underline{\Theta}_q \cdot \underline{x}}[2\mu_L(\underline{\Theta}_q \otimes \underline{\Theta}_q) + \lambda_L \underline{n}] \tag{38}$$

and for shear waves

$$\underline{\underline{\sigma}}(\underline{\Theta}_q^\perp e^{ik_s \underline{\Theta}_q \cdot \underline{x}})\underline{n} = ik_s e^{ik_s \underline{\Theta}_q \cdot \underline{x}} \mu_L[(\underline{\Theta}_q^\perp \otimes \underline{\Theta}_q) + (\underline{\Theta}_q \otimes \underline{\Theta}_q^\perp)]\underline{n}, \tag{39}$$

where $\otimes$ denotes the tensor product.

When designing a particular DEM element, a balance must be struck between the quality of the Lagrange multiplier approximation, which in general improves as their number is increased, and numerical stability and cost concerns.

Next, two elastic wave propagation DEM elements of increasing order of accuracy are presented as examples of the discretization methodology outlined above. For the sake of simplicity, only regular hexahedral geometries are considered. Generalizing these elements to the case of arbitrary hexahedral geometries is a straightforward task (for example, see [5]).

- **H–(26×3)–15.** The directions $\underline{\Theta}_q$, $q = 1, \ldots, 26$ of propagation of the pressure and shear waves for this element coincide with those of the Helmholtz DGM element H-26-4. They may be concisely written as follows. Define

$$\Theta = \begin{bmatrix} 1 & 0 & 0 & 1 & 1 & 1 & -1 & 1 & 1 & 0 & 1 & 1 & 0 \\ 0 & 1 & 0 & 1 & 1 & -1 & 1 & 1 & 0 & 1 & -1 & 0 & 1 \\ 0 & 0 & 1 & 1 & -1 & 1 & 1 & 0 & 1 & 1 & 0 & -1 & -1 \end{bmatrix}$$

and

$$\Theta^{\perp} = \begin{bmatrix} 0 & 1 & 1 & 0 & 0 & 0 & 1 & 0 & 0 & 1 & 0 & 0 & 1 \\ 1 & 0 & 0 & -1 & 1 & 1 & 1 & 0 & 1 & 0 & 0 & 1 & 0 \\ 0 & 0 & 0 & 1 & 1 & 1 & -1 & 1 & 0 & 0 & 1 & 0 & 0 \end{bmatrix}.$$

Let $\underline{\phi}_q$ and $\underline{\phi}_q^{\perp}$, $q = 1, \ldots, 26$ denote the q–th columns of the matrix $[\Theta, -\Theta]$ and $[\Theta^{\perp}, -\Theta^{\perp}]$ respectively. Then, the directions and polarizations of the waves in (34) are for $q = 1, \ldots, 26$,

$$\underline{\Theta}_q = \frac{\underline{\phi}_q}{||\underline{\phi}_q||}, \quad \underline{\Theta}_q^{\perp} = \frac{\underline{\phi}_q^{\perp}}{||\underline{\phi}_q^{\perp}||}, \quad \underline{\Theta}_q^{\perp\perp} = \underline{\phi}_q \times \underline{\phi}_q^{\perp}. \tag{40}$$

In order to describe the Lagrange multipliers of this element, a local coordinate system is defined on each face in such a way that the x and y axes are aligned with the sides of the face, and the z axis is normal to the face. Fifteen Lagrange multipliers per face are defined, of which one is of pressure type and 14 are based on tractions of shear waves. Let $n^{\lambda_p} = 1$, $n^{\lambda_s} = 14$,

$$\Theta_{pressure} = \begin{bmatrix} 0 \\ 0 \\ 1 \end{bmatrix},$$

$$\Theta_{shear} = \begin{bmatrix} 0 & 0 & 1 & -1 & 1 & -1 & 1 & -1 & 1 & -1 & 1 & -1 & 1 & -1 \\ 0 & 0 & 1 & -1 & -1 & 1 & 1 & -1 & -1 & 1 & 1 & 1 & -1 & -1 \\ 1 & 1 & \sqrt{2} & \sqrt{2} & \sqrt{2} & \sqrt{2} & \sqrt{2} & \sqrt{2} & \sqrt{2} & \sqrt{2} & 0 & 0 & 0 & 0 \end{bmatrix},$$

and

$$\Theta_{shear}^{\perp} = \begin{bmatrix} 1 & 0 & 1 & 1 & 1 & 1 & \sqrt{2} & \sqrt{2} & \sqrt{2} & \sqrt{2} & 0 & 0 & 0 & 0 \\ 0 & 1 & -1 & -1 & 1 & 1 & \sqrt{2} & \sqrt{2} & -\sqrt{2} & -\sqrt{2} & 0 & 0 & 0 & 0 \\ 0 & 0 & 0 & 0 & 0 & 0 & -2 & 2 & -2 & 2 & 1 & 1 & 1 & 1 \end{bmatrix}.$$

Then, the explicit representation of the Lagrange multipliers is obtained by transforming each column of $\Theta_{pressure}$ and corresponding columns of Θ_{shear} and $\Theta_{shear}^{\perp}$ into the global frame, normalizing them to unity and using the relations (38) and (39), respectively. The pressure Lagrange multiplier and the first two of the shear Lagrange multipliers are based on waves propagating in the normal direction to the face and give rise to constant tractions. The last four of the Lagrange multipliers are based on shear waves propagating in the plane of the face. The remaining eight multipliers are based on waves directed at the face at a 45° cone angle (see Figure 3). This specific cone angle has a special importance as the corresponding tractions are invariant when the normal is flipped, which makes the element "symmetric" without the need for adding multipliers in the directions with the opposite z component.

- **H–(50×3)–28.** This element uses 50 pressure waves and 100 shear waves in the enrichment field. The enrichment functions are defined as for the previous element and are based on the matrices

$$\Theta = \left[\begin{array}{cccccccccccccc} 1 & 0 & 0 & 1 & 1 & 1 & -1 & 1 & 1 & 0 & 1 & 1 & 0 & 1 \\ 0 & 1 & 0 & 1 & 1 & -1 & 1 & 1 & 0 & 1 & -1 & 0 & 1 & -1/2 \\ 0 & 0 & 1 & 1 & -1 & 1 & 1 & 0 & 1 & 1 & 0 & -1 & -1 & -1/2 \end{array}\right. \ldots$$

$$\left.\begin{array}{cccccccccccc} 1 & 1 & 1 & -1/2 & -1/2 & 1/2 & 1/2 & -1/2 & -1/2 & 1/2 & 1/2 \\ -1/2 & 1/2 & 1/2 & 1 & 1 & 1 & 1 & -1/2 & 1/2 & -1/2 & 1/2 \\ 1/2 & -1/2 & 1/2 & -1/2 & 1/2 & -1/2 & 1/2 & 1 & 1 & 1 & 1 \end{array}\right]$$

and

$$\Theta^{\perp} = \left[\begin{array}{ccccccccccccc} 0 & 1 & 1 & 0 & 0 & 0 & 0 & 0 & 0 & 1 & 0 & 0 & \\ 1 & 0 & 0 & -1 & 1 & 1 & 1 & 0 & 1 & 0 & 0 & 1 & \ldots \\ 0 & 0 & 0 & 1 & 1 & 1 & -1 & 1 & 0 & 0 & 1 & 1 & \end{array}\right.$$

$$\left.\begin{array}{ccccccccccccc} 1 & 0 & 0 & 0 & 0 & 1 & 1 & 1 & 1 & 1 & 1 & 1 & 1 \\ \ldots\ 0 & 1 & 1 & 1 & 1 & 0 & 0 & 0 & 0 & -1 & 1 & 1 & -1 \\ 0 & -1 & 1 & 1 & -1 & -1 & 1 & 1 & -1 & 0 & 0 & 0 & 0 \end{array}\right].$$

The Lagrange multipliers are constructed in a manner similar to that described for the previous element. More specifically, there are eight Lagrange multipliers per face that are based on tractions of pressure waves which propagate at an angle to the face

$$\Theta_{pressure} = \left[\begin{array}{cccccccc} 1 & -1 & 0 & 0 & 1 & -1 & 0 & 0 \\ 0 & 0 & 1 & -1 & 0 & 0 & 1 & -1 \\ 2 & 2 & 2 & 2 & -2 & -2 & -2 & -2 \end{array}\right].$$

There are also 20 Lagrange multipliers per face that are based on tractions of shear waves. Compared to the case of the previous element, there are additional eight multipliers that are based on 45-degree shear waves

$$\Theta_{shear} = \left[\begin{array}{cccccccccccc} 1 & -1 & 0 & 0 & 1 & -1 & 0 & 0 & 1 & -1 & 1 & \\ 0 & 0 & 1 & -1 & 0 & 0 & 1 & -1 & 1 & -1 & -1 & \ldots \\ 1 & 1 & 1 & 1 & 1 & 1 & 1 & 1 & \sqrt{2} & \sqrt{2} & \sqrt{2} & \end{array}\right.$$

$$\left.\begin{array}{ccccccccccc} -1 & 1 & -1 & 1 & -1 & 1 & -1 & 1 & -1 \\ \ldots\ 1 & 1 & -1 & -1 & 1 & 1 & 1 & -1 & -1 \\ \sqrt{2} & \sqrt{2} & \sqrt{2} & \sqrt{2} & \sqrt{2} & 0 & 0 & 0 & 0 \end{array}\right]$$

and

$$\Theta_{shear}^{\perp} = \left[\begin{array}{cccccccccccc} 0 & 0 & 1 & 1 & -1 & 1 & 0 & 0 & 1 & 1 & 1 & 1 \\ 1 & 1 & 0 & 0 & 0 & 0 & -1 & 1 & -1 & -1 & 1 & 1 \\ 0 & 0 & 0 & 0 & 1 & 1 & 1 & 1 & 0 & 0 & 0 & 0 \end{array}\right. \ldots$$

$$\left.\begin{array}{cccccccc} \sqrt{2} & \sqrt{2} & \sqrt{2} & \sqrt{2} & 0 & 0 & 0 & 0 \\ \ldots\ \sqrt{2} & \sqrt{2} & -\sqrt{2} & -\sqrt{2} & 0 & 0 & 0 & 0 \\ -2 & 2 & -2 & -2 & 1 & 1 & 1 & 1 \end{array}\right].$$

The aforementioned waves are graphically depicted in Figure 3.

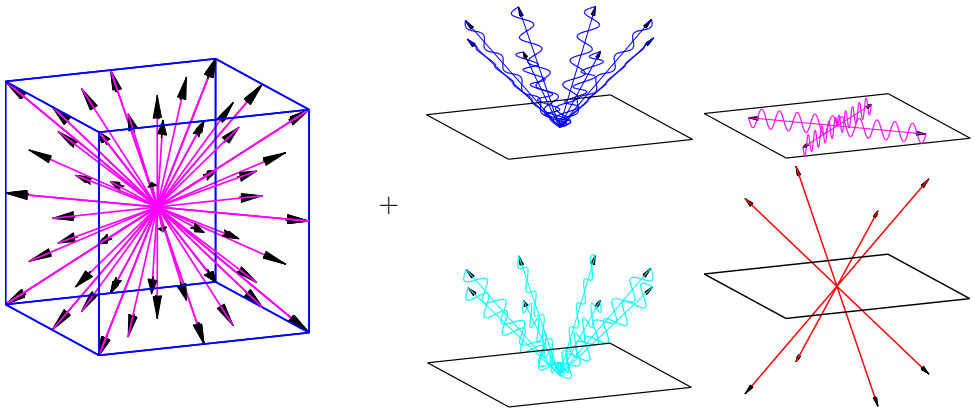

Figure 3. DEM element H–(50×3)–28: directions of the enrichment field for the solution, and generating waves for the Lagrange multipliers.

When required, the new H–(26×3)–15 and H–(50×3)–28 DEM elements described above can also be equipped with a polynomial field. Without it, their sparsity pattern and number of degrees of freedom are such that, from a computational complexity viewpoint, they are equivalent to the quadratic and cubic p-type (polynomial) standard Galerkin elements, respectively. The performances of these new DEM elements are assessed in Section 5 for a coupled fluid-solid problem.

Wave propagation problems with fluid/fluid, fluid/solid, or solid/solid interfaces give rise however to multiscale wave propagation problems with evanescent waves that have different characteristics than the traveling waves on which the DGM/DEM elements covered so far are based on. For this reason, the DEM/DGM elements outlined above, and summarily labeled here H–X–Y, are further enriched in the following sections to improve their efficiency when applied to the solution of wave propagation problems with evanescent waves. Similar ideas have been previously explored in [8] in two dimensions. They are here presented in three dimensions. The resulting elements are labeled H–X–Y* and designed for usage in the vicinity of material interfaces..

3.3. DGM elements for fluid/fluid interface regions

Consider the case of two semi-infinite fluids with computational subdomains Ω_{f_1} and Ω_{f_2} separated by a planar interface as illustrated in Figure 4a. When an incident wave $p_{\rm inc}$ impinges on the interface from the Ω_{f_1} side in an oblique direction and the two fluids have different speeds of sound, it produces a reflected wave $p_{\rm r}$ in Ω_{f_1} and a refracted wave p_t in Ω_{f_2}. The relationship between the altitude angle of the incident wave $\theta_{\rm inc}$ (see Figure 4), the altitude angle of the refracted wave $\theta_{\rm t}$ (see Figure 4), and the speeds of sound in the two fluids, c_1 and c_2, is known as Snell's law [10] and is recalled below

$$\frac{\cos\theta_{\rm inc}}{c_1} = \frac{\cos\theta_t}{c_2}. \tag{41}$$

When $c_1 < c_2$, Snell's law predicts that the altitude angle of the refracted wave is smaller than that of the incident wave, i.e. $\theta_t < \theta_{\rm inc}$. As the altitude angle of incidence is decreased,

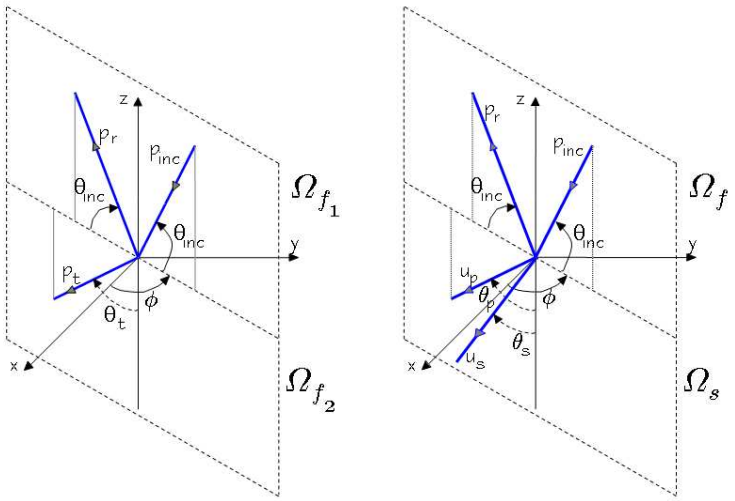

(a) fluid/fluid domain (b) fluid/solid domain

Figure 4. Incident, reflected, and refracted waves in fluid/fluid (a) and fluid/solid (b) media.

the refracted wave eventually becomes parallel to the interface. This occurs for one particular altitude angle of incidence called the *critical angle* and given by

$$\theta_{\rm cr} = \cos^{-1}\left(\frac{c_1}{c_2}\right), \quad \text{if} \quad c_1 < c_2. \tag{42}$$

If $\theta_{\rm inc} < \theta_{\rm cr}$, the refracted wave disappears, the incident wave undergoes *total internal reflection* and an *evanescent wave* occurs in the second fluid, Ω_{f_2}.

For simplicity, assume that the coordinate system is such that the interface is the x–y plane, Ω_{f_1} is the region $z > 0$, and Ω_{f_2} is the region $z < 0$. Furthermore, assume that $p_{\rm inc}$, p_r and p_t are plane waves that satisfy the Helmholtz equation (4) in their respective domains. From the transmission conditions

$$p_{inc} + p_r = p_t \quad \text{and} \quad \frac{1}{\rho_1}\frac{\partial}{\partial \underline{n}}\left(p_{inc} + p_r\right) = \frac{1}{\rho_2}\frac{\partial p_t}{\partial \underline{n}},$$

it follows that these plane waves are of the form

$$p_{\rm inc} = A_{\rm inc} e^{ik_1\left((x\cos\phi + y\sin\phi)\cos\theta_{\rm inc} - z\sin\theta_{\rm inc}\right)}, \tag{43}$$

$$p_r = A_r e^{ik_1\left((x\cos\phi + y\sin\phi)\cos\theta_{\rm inc} + z\sin\theta_{\rm inc}\right)}, \tag{44}$$

$$p_t = A_t e^{\beta z} e^{i\sqrt{k_2^2+\beta^2}(x\cos\phi + y\sin\phi)}, \tag{45}$$

where $\beta = \sqrt{k_1^2\cos^2\theta_{\rm inc} - k_2^2}$ and the amplitudes $A_{\rm inc}$, A_r and A_t are given by

$$A_r = -\frac{\rho_1\beta + ik_1\rho_2\sin\theta_{\rm inc}}{\rho_1\beta - ik_1\rho_2\sin\theta_{\rm inc}}A_{\rm inc}, \qquad A_t = -\frac{2ik_1\rho_2\sin\theta_{\rm inc}}{\rho_1\beta - ik_1\rho_2\sin\theta_{\rm inc}}A_{\rm inc}. \tag{46}$$

Hence, β is a real number if $\theta_{\text{inc}} < \theta_{\text{cr}}$, in which case the transmitted (refracted or evanescent) wave p_t is evanescent and decays exponentially in the negative z direction. Note also that the apparent wave number of the evanescent wave p_t along the interface is $\alpha \in [k_2, k_1]$, instead of the native wave number k_2.

Next, new DGM elements H–X–Y* are constructed by further enriching the H–X–Y (see Section 3.1) elements with evanescent waves. More specifically, the wave approximation of the solution and its corresponding Lagrange multiplier field are rewritten, element by element, and face by face as

$$p_h^E(\underline{x}) = p_h^{PW}(\underline{x}) + p_h^{EW}(\underline{x}) \quad \text{and} \quad \lambda_h(\underline{x}) = \lambda_h(\underline{x})^{PW} + \lambda_h(\underline{x})^{EW}. \tag{47}$$

The superposition of planar waves $p_h^{PW}(\underline{x})$ is given by (31). The enrichment field $p_h^{EW}(\underline{x})$ is chosen as a superposition of evanescent waves that propagate along the fluid/fluid interface and decay away from it. If the element is assumed — for the sake of simplicity of notation — to be a cube aligned with the coordinate system, then

$$p_h^{EW}(\underline{x}) = \sum_{j=1}^{n^{ev}} p_j e^{i\underline{k}_j^{ev}\cdot\underline{x}} \tag{48}$$

where n^{ev} is the number of evanescent enrichment waves and $\underline{k}_j^{ev} = [\alpha\cos\phi_j, \alpha\sin\phi_j, i\beta]$. The real constants α and β are given by

$$\alpha = k_1\cos\theta^{EW}, \qquad \beta = \sqrt{k_1^2\cos^2\theta^{EW} - k_2^2}, \tag{49}$$

where θ^{EW} is a subcritical altitude angle that is set *a priori*.

Following the same approach adopted for the design of λ_h^{PW}, the Lagrange multiplier field λ_h^{EW} is chosen as the following approximation of $\partial p_h^{EW}/\partial\underline{n}$

$$\lambda_h^{EW} = \begin{cases} \sum_{j=1}^{n^{\lambda_{ev}}} \lambda_j^{EW} e^{i\alpha(x\cos\phi_j + y\sin\phi_j)} & \text{on horizontal faces,} \\ \lambda_0^{EW} e^{\beta z} & \text{on vertical faces.} \end{cases} \tag{50}$$

Different choices of θ^{EW} and the number and values of the directions ϕ_j of the evanescent waves (see Figure 5 and Figure 6) lead to different elements with different computational efficiencies. Four possible choices leading to four new DGM elements are discussed below. These new elements are labeled H–26–Y* and H–56–Y* because they are constructed by further enriching in different ways the DGM elements H–26–4 and H–56–8, respectively (Section 3.1).

- **H–26–4***. Here, $n^{ev} = 4$, $n^{\lambda_{ev}} = 4$ on the horizontal faces, and $n^{\lambda_{ev}} = 1$ on the vertical ones. The evanescent enrichment waves are defined by (48) and the azimuthal angles
$$\phi_j = \frac{\pi}{4} + (j-1)\frac{\pi}{2}, \qquad j = 1, \ldots, 4\ .$$
The evanescent Lagrange multipliers are constructed using the same angles and (50).
- **H–26–4****. For this element, $n^{ev} = 4$, $n^{\lambda_{ev}} = 4$ on the horizontal faces, and $n^{\lambda_{ev}} = 1$ on the vertical faces. The enrichment for evanescent wave problems is the same as in the previous element. However, the azimuthal angles for the multipliers are different and chosen as follows
$$\phi_j = (j-1)\frac{\pi}{2}, \qquad j = 1, \ldots, 4\ .$$

- **H–26–8***. Here, $n^{ev} = 8$, $n^{\lambda_{ev}} = 8$ on the horizontal faces, and $n^{\lambda_{ev}} = 1$ on the vertical ones. This DGM element uses a set of eight directions for the evanescent enrichment. Its Lagrange multipliers are given by the following azimuthal angles

$$\phi_j = (j-1)\frac{\pi}{4}, \qquad j = 1, \ldots, 8 \ .$$

- **H–56–8***. For this element, $n^{ev} = 8$, $n^{\lambda_{ev}} = 8$ on the horizontal faces, and $n^{\lambda_{ev}} = 1$ on the vertical faces. This DGM element uses the same enrichment for capturing evanescent waves as the previous element, but is based on the element H–56–8.

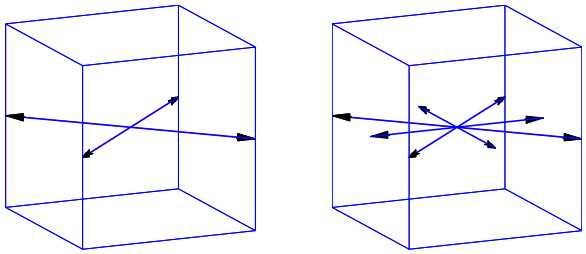

(a) (b)

Figure 5. Directions of the evanescent wave enrichment functions for the solution.

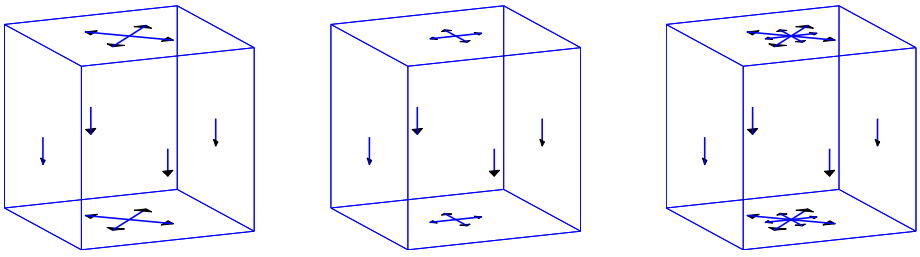

(a) (b) (c)

Figure 6. Directions of the evanescent wave functions for the Lagrange multipliers.

3.4. DEM elements for fluid/solid interface regions

When an incident wave p_{inc} encounters a fluid/solid interface, it gives rise to two transmitted waves in the solid: a pressure wave $\underline{u}_p$ and a shear wave $\underline{u}_s$, as shown in Figure 4b. In this situation, Snell's law states that

$$\frac{\cos\theta_{\text{inc}}}{c_f} = \frac{\cos\theta_p}{c_p} = \frac{\cos\theta_s}{c_s}, \tag{51}$$

where $\theta_{\rm inc}$ is the altitude angle of the incident wave, θ_p and θ_s are the altitude angles of the refracted pressure and shear waves, respectively, c_f is the speed of sound in the fluid, and c_p and c_s are the elastic speeds of sound in the solid given by

$$c_p = \frac{\omega}{k_p}, \quad c_s = \frac{\omega}{k_s}, \tag{52}$$

where k_p and k_s are given by (35).

There are two critical angles: $\theta_{\rm cp}$ for pressure waves, and $\theta_{\rm cs}$ for shear waves. These angles are given by

$$\theta_{\rm cp} = \cos^{-1}(\frac{c_f}{c_p}), \quad \text{if } c_f < c_p, \quad \text{and} \quad \theta_{\rm cs} = \cos^{-1}(\frac{c_f}{c_s}), \quad \text{if } c_f < c_s. \tag{53}$$

Assume that the interface is aligned with the x–y plane, Ω_f is the region $z > 0$, Ω_s is the region $z < 0$, and the incident, reflected, and transmitted waves are in the form of plane waves. In this case, using the transmission conditions (6) and (7), it can be shown that the transmitted pressure wave $\underline{u}_p$ is evanescent if $c_f < c_p$ and $\theta_{\rm inc} < \theta_{\rm cp}$, the transmitted shear wave $\underline{u}_s$ is evanescent if $c_f < c_s$ and $\theta_{\rm inc} < \theta_{\rm cs}$, and these waves are of the form

$$p_{\rm inc} = A_{\rm inc} e^{ik([x\cos\phi + y\sin\phi]\cos\theta_{\rm inc} - z\sin\theta_{\rm inc})}, \tag{54}$$

$$p_r = A_r e^{ik([x\cos\phi + y\sin\phi]\cos\theta_{\rm inc} + z\sin\theta_{\rm inc})}, \tag{55}$$

$$\underline{u}_p = A_p \begin{bmatrix} \alpha\cos\phi \\ \alpha\sin\phi \\ i\beta \end{bmatrix} e^{\beta z} e^{i\alpha[x\cos\phi + y\sin\phi]}, \tag{56}$$

$$\underline{u}_s = A_s \begin{bmatrix} -ib\cos\phi \\ -ib\sin\phi \\ a \end{bmatrix} e^{bz} e^{ia[x\cos\phi + y\sin\phi]}, \tag{57}$$

where

$$\alpha^2 = \beta^2 + k_p^2, \qquad \beta = \sqrt{k^2\cos^2\theta_{\rm inc} - k_p^2}, \tag{58}$$

$$a^2 = b^2 + k_s^2, \qquad b = \sqrt{k^2\cos^2\theta_{\rm inc} - k_s^2}, \tag{59}$$

and the amplitudes are given by

$$A_s = -\frac{2i\alpha k\sin\theta_{\rm inc}}{\rho_f\omega^2(2\alpha a - a^2 + b^2) - i2\alpha k\sin\theta_{\rm inc}} A_{\rm inc}, \tag{60}$$

$$A_p = -\frac{a^2 - b^2}{2\alpha\beta} A_s, \tag{61}$$

$$A_r = -i(k_p^2\lambda_L + 2\beta^2\mu_L)A_p - 2iab\mu_L A_s - A_{\rm inc}. \tag{62}$$

Hence, the evanescent waves $\underline{u}_p$ and $\underline{u}_s$ decay exponentially in the negative z direction.

Following the same procedure outlined previously for fluid type (Helmholtz) DGM elements, the approximate solution in the solid type (Navier) DEM elements for elastodynamic problems can be further enriched for capturing evanescent waves as follows

$$\underline{u}_h^E = u_h^{PW}(\underline{x}) + u_h^{EW}(\underline{x}) \tag{63}$$

where $u_h^{PW}(\underline{x})$ is the same as in (34), and the evanescent enrichment is chosen as

$$u_h^{EW}(\underline{x}) = \sum_{j=1}^{n^E} \underline{u}_{p_j} \begin{bmatrix} \alpha\cos\phi_j \\ \alpha\sin\phi_j \\ i\beta \end{bmatrix} e^{\beta z} e^{i\alpha(x\cos\phi_j + y\sin\phi_j)} + \sum_{j=1}^{n^E} \underline{u}_{s_j} \begin{bmatrix} -ib\cos\phi_j \\ -ib\sin\phi_j \\ a \end{bmatrix} e^{bz} e^{ia(x\cos\phi_j + y\sin\phi_j)} \tag{64}$$

where

$$\beta = \sqrt{k^2\cos^2\theta^{EW} - k_p^2}, \quad \alpha^2 = k_p^2 + \beta^2, \tag{65}$$

$$b = \sqrt{k^2\cos^2\theta^{EW} - k_s^2}, \quad a^2 = k_s^2 + b^2. \tag{66}$$

As in the case of a fluid/fluid interface, the Lagrange multiplier field is approximated by $\underline{\lambda}_h = \underline{\lambda}_h^{PW} + \underline{\lambda}_h^{EW}$, where $\underline{\lambda}_h^{PW}$ is chosen in the space Λ_h^s specified in the expression (37), and $\underline{\lambda}_h^{EW}$ is chosen as the traction $\underline{\underline{\sigma}}(\underline{u}_h^{EW})\underline{n}$.

Evanescent waves can also potentially arise on the fluid side of a fluid/solid interface, depending on the material properties. They can then be captured by the elements described in the previous section with the wave number k_1 in the fluid replaced by the pressure wave number k_p and/or the shear wave number k_s of the solid.

As an example, two new DEM elements are constructed below assuming again — for the sake of simplicity of notation — that the element is a cube aligned with the coordinate system. The new elements are derived from the H–(26×3)–15 and H–(50×3)–28 elements, respectively, by adding a total of 16 evanescent waves to the enrichment field, eight of which are pressure waves and eight of which are shear waves, using the definition (64) with $n^E = 8$ and the azimuthal angles

$$\phi_j = (j-1)\frac{\pi}{4}, \qquad j = 1, \ldots, 8\ .$$

In order to not over-constrain the final system and avoid numerical instability, only four evanescent Lagrange multipliers are added on the horizontal faces. They are obtained by computing the traction of the evanescent shear waves given by the directions $\phi_j = [0, \pi/2, \pi, 3\pi/2]$. Thus, for the Lagrange multipliers on the horizontal faces, one obtains

$$\begin{aligned} \lambda^{EW} = \quad & \lambda_1^{EW} \begin{bmatrix} i(a^2-b^2) \\ 0 \\ 2ab \end{bmatrix} e^{iax} + \lambda_2^{EW} \begin{bmatrix} 0 \\ i(a^2-b^2) \\ 2ab \end{bmatrix} e^{iay} + \\ & \lambda_3^{EW} \begin{bmatrix} i(a^2-b^2) \\ 0 \\ -2ab \end{bmatrix} e^{-iax} + \lambda_4^{EW} \begin{bmatrix} 0 \\ i(a^2-b^2) \\ -2ab \end{bmatrix} e^{-iay}\ . \end{aligned}$$

On the vertical faces aligned with the x–z plane and the y–z plane, the following multipliers with a decaying component are obtained

$$\lambda^{EW} = \lambda_1^{EW} \begin{bmatrix} 2ab \\ 0 \\ i(a^2-b^2) \end{bmatrix} e^{iax} e^{bz} + \lambda_2^{EW} \begin{bmatrix} -2ab \\ 0 \\ i(a^2-b^2) \end{bmatrix} e^{-iax} e^{bz},$$

and

$$\lambda^{EW} = \lambda_1^{EW} \begin{bmatrix} 0 \\ 2ab \\ i(a^2-b^2) \end{bmatrix} e^{iay} e^{bz} + \lambda_2^{EW} \begin{bmatrix} 0 \\ -2ab \\ i(a^2-b^2) \end{bmatrix} e^{-iay} e^{bz}.$$

4. NUMERICAL RESULTS

In this section, the performance of the newly constructed DGM elements with evanescent wave enrichment functions is assessed and compared to that of their counterparts without this additional type of enrichment functions, and to the performance of comparable standard higher-order polynomial finite elements. For this purpose, fluid-fluid and fluid-solid wave propagation benchmark problems with known analytical solutions which furthermore justify dropping the polynomial field from the enriched approximation are considered.

It is recalled that in [7], it was shown that:

1. The DGM element H–26–4 has a computational complexity and a convergence rate that are comparable to those of the standard quadratic Galerkin element Q_2, but a significantly smaller error constant and therefore a significantly better accuracy.
2. The DGM element H–56–8 has a computational complexity and a convergence rate that are comparable to those of the standard cubic Galerkin element Q_3 , but a significantly smaller error constant and therefore a significantly better accuracy.

Hence, the performances compared here are those of the elements H–26–4, H–26–4* and Q_2, and those of the elements H–56–8, H–56–8* and Q_3.

In the strict sense, the performance of a discretization method applied to the solution of the family of problems considered in this section depends on the direction of the incident wave. For this reason, all benchmark problems discussed in this section are conducted as follows. For each specified altitude angle of incidence θ_{inc}, five computations are performed for the following five different values of the azimuthal angle of incidence

$$\phi_{\text{inc}} = 0^\circ,\ \phi_{\text{inc}} = 11.25^\circ,\ \phi_{\text{inc}} = 22.5^\circ,\ \phi_{\text{inc}} = 33.75^\circ,\ \text{and}\ \phi_{\text{inc}} = 45^\circ.$$

The sampling in the interval $[0^\circ,\ 45^\circ]$ is due to the azimuthal symmetry of the considered benchmark problems. The five obtained relative errors are then simply averaged and the result is reported as the relative error associated with the specified value of θ_{inc}.

For DGM, the degree of freedom count is based only on the total number of Lagrange multipliers, because of the static condensation property of these elements. Since the internal degrees of freedom of the standard higher-order Galerkin elements can also be condensed out at the element level, they are also not included in the degree of freedom count in order to provide meaningful performance comparisons.

Because evanescent waves decay exponentially away from the interface, adding them into the approximation space of the elements located far away from the interface may not be necessary. Therefore, the evanescent wave enrichment degrees of freedom and corresponding Lagrange multipliers are activated only in the two layers of elements that are closest to the interface, as shown in Figure 7. Also, due to the exponential decay of the function $e^{\beta z}$ in in the direction $z < 0$, the inclusion of evanescent waves in a basis can result in nearly singular local stiffness matrices, particularly in the elements further away from the interface. To prevent this from happening, the scaling technique used for the evanescent waves in two dimensions [8] is adopted here — that is, the evanescent wave enrichment functions are scaled so that their maximum amplitude is equal to one in each element. The same scaling technique is applied to the corresponding approximation of the Lagrange multiplier field on each element face.

4.1. Acoustic evanescent waves

The domain $\Omega = [0,1] \times [0,0.25] \times [-0.25,0.25]$ is divided into two subdomains: $\Omega_{f_1} = [0,1] \times [0,0.25] \times [-0.25,0]$ and $\Omega_{f_2} = [0,1] \times [0,0.25] \times [0,0.25]$, which are assumed to be filled with water ($\rho_1 = 1.29\text{kg/m}^3$, $c_1 = 343\text{m/s}$) and air ($\rho_2 = 1000\text{kg/m}^3$, $c_2 = 1533\text{m/s}$), respectively. The Robin boundary condition (9) is applied on the boundaries Γ_{f_m}, $m = 1,2$, with $g_m = \dfrac{\partial p_m^{\text{ex}}}{\partial n} - ik_m p_m^{\text{ex}}$, where the two components of the exact solution $p_1^{\text{ex}} = p_{\text{inc}} + p_r$ in Ω_{f_1} and $p_2^{\text{ex}} = p_t$ in Ω_{f_2} are shown in Figure 4. The incident wave p_{inc}, the reflected wave p_r, and the transmitted waves are given by Eqs. (43–46). For this problem setup, the critical angle is $\theta_{\text{cr}} = 77.16°$. The wave numbers $k_1 = \omega/c_1$ and $k_2 = \omega/c_2$ and the altitude angle of the incident wave θ_{inc} considered for this problem are specified later in this section.

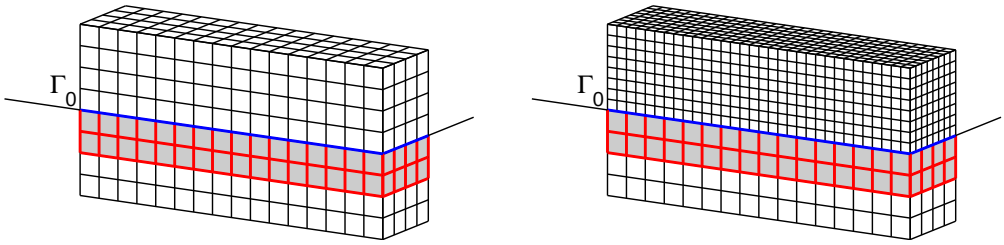

Figure 7. Discretization of the computational subdomains associated with a fluid-fluid or fluid-solid problem: same mesh size scenario (left), and coarse-fine meshes scenario (right). Elements with evanescent wave enrichment functions are used only in the first two layers of the bottom subdomain and colored in grey.

The two computational subdomains are discretized uniformly (see Figure 7). For each assessed numerical solution method, the mesh size is varied in order to enable a mesh convergence numerical study. Since c_1 is smaller than c_2, a coarser mesh may be used in subdomain Ω_{f_2} if a constant number of elements per wavelength is adopted. Thus, two types of subdomain meshes are considered as shown in Figure 7: (a) same size meshes, (b) coarse-fine meshes where the mesh in Ω_{f_2} is twice coarser than that in Ω_{f_1}. Since by construction, the DGM elements incorporate Lagrange multipliers on their interfaces in order to enforce there a weak continuity of the solution, their usage on non-matching meshes as in the coarse-fine discretization scenario requires no special attention. On the other hand, the eventual usage of standard Galerkin elements in the coarse-fine discretization scenario would require the introduction of mortar elements at the fluid-fluid interface and therefore is not considered here.

In all computations reported for this problem, θ^{EW} is set to

$$\theta^{EW} = \frac{1}{2}\theta_{\text{cr}} = 38.58°.$$

The discretization error is measured separately in each of the two computational subdomains $\Omega_{fm}, m = 1,2$. The relative error associated with the classical FEM is measured by the discrete

L_2 norm over all vertices in the subdomains — that is, by

$$\frac{\|p^{\text{ex}} - p_h^{\text{FEM}}\|_{\Omega_{fm}}}{\|p^{\text{ex}}\|_{\Omega_{fm}}} = \frac{\sqrt{\sum_{V \in \Delta^m_{\text{vert}}} |(p^{\text{ex}} - p_h^{\text{FEM}})(V)|^2}}{\sqrt{\sum_{V \in \Delta^m_{\text{vert}}} p^{\text{ex}}(V)^2}}, \tag{67}$$

where Δ^m_{vert} denotes the set of all vertices in the mesh $\Delta^m_h, m = 1, 2$. The relative error associated with a DGM solution is measured using the same metric. However, since the DGM solution is discontinuous at the vertices, it is first averaged as follows

$$\tilde{p}_h^{\text{DGM}}(V) = \frac{1}{n^m_{\text{vert}}} \sum_{\substack{\tau \in \Delta^m_h \\ V \in \tau}} p_h^{\text{DGM}}|_\tau(V), \tag{68}$$

where $n^m_{\text{vert}}, m = 1, 2$, denotes the number of elements in subdomain Ω_{fm} sharing the vertex V. Then, the corresponding relative error is computed as follows

$$\frac{\|p^{\text{ex}} - p_h^{\text{DGM}}\|_{\Omega_{fm}}}{\|p^{\text{ex}}\|_{\Omega_{fm}}} = \frac{\sqrt{\sum_{V \in \Delta^m_{\text{vert}}} |(p^{\text{ex}} - \tilde{p}_h^{\text{DGM}})(V)|^2}}{\sqrt{\sum_{V \in \Delta^m_{\text{vert}}} p^{\text{ex}^2}}}. \tag{69}$$

Figure 8 reports the convergence rates of the original DGM element H–26–4, its three versions that are enriched with evanescent wave functions H–26–Y*, H–26–Y**, and H–26–8*, and the standard Galerkin element Q_2, in the medium frequency regime $k_1 = 60$ and $k_2 = 13.33$ and for the subcritical altitude angle of incidence $\theta_{inc} = 25^\circ$. This altitude angle of incidence gives rise to evanescent waves in Ω_{f_2}. As expected, the results reported in this figure show that the selective inclusion of evanescent waves in the enrichment field of the DGM elements in the vicinity of the fluid-fluid interface on the Ω_{f_2} side: (1) is a good strategy, (2) improves dramatically the performance of the DGM elements in subdomain Ω_{f_2} where evanescent waves are created, and (3) improves only a little the performance of the DGM elements in subdomain Ω_{f_1} where the exact solution does not contain any evanescent wave. More specifically, the DGM element H–26–4 is found to improve the accuracy of the standard element Q_2 in the subdomain Ω_{f_1} by almost a full order of magnitude, which is consistent with the results previously established for a homogeneous fluid domain [7]. However, more importantly, portions (b) and (d) of Figure 8 show that in subdomain Ω_{f_2} where evanescent waves arise, the DGM element H–26–4 element fails even to match the performance of the standard element Q_2, which indicates that a basis of planar wave functions is not quite able to capture the exponential decay of the solution there. On the other hand, all versions of this DGM element that feature further enrichment by evanescent wave functions are reported to outperform the standard quadratic element Q_2. For example, the DGM element H–26-8* reaches the 2% level of relative error in subdomain Ω_{f_2} using five times fewer degrees of freedom than Q_2 for the matching meshes scenario. For the coarse-fine mesh scenario that is natural for the DGM technology, the DGM element H–26-8* reaches the same 2% level of relative error in Ω_{f_2} using 12 times fewer degrees of freedom than Q_2.

Next, the two wave numbers are increased to $k_1 = 90$ and $k_2 = 20.14$. Accordingly, the DGM elements H–56–8 and H–56–8*, and the standard Galerkin element Q_3 are considered

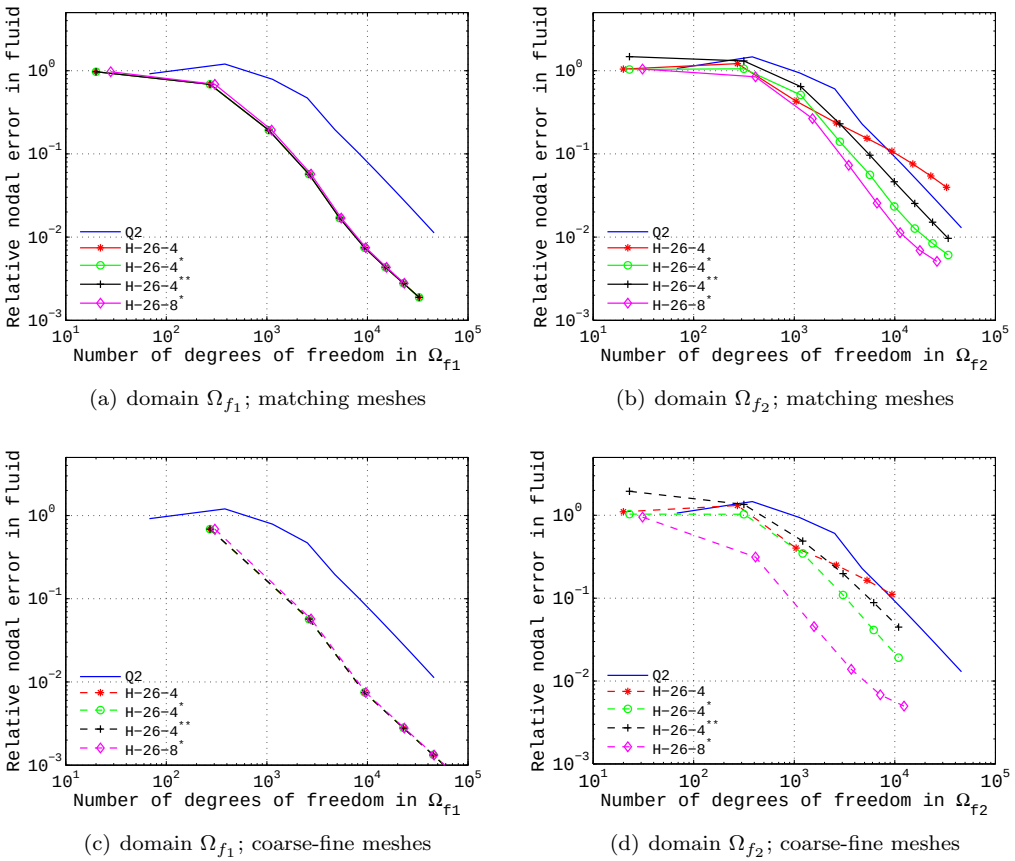

(a) domain Ω_{f_1}; matching meshes

(b) domain Ω_{f_2}; matching meshes

(c) domain Ω_{f_1}; coarse-fine meshes

(d) domain Ω_{f_2}; coarse-fine meshes

Figure 8. Fluid-fluid wave propagation model problem: comparison of the performances of the elements H–26–Y*, H–26–4, and Q_2 for $k_1 = 60$, $k_2 = 13.33$ and $\theta_{inc} = 25°$.

for the discretization of the problem at hand. The results obtained for the scenario of matching meshes are reported in Figure 9. As in the previous case of lower frequency, the DGM element H–56–8 is found to outperform the cubic element in Ω_{f_1}; more specifically it delivers the same accuracy using seven times fewer degrees of freedom. However, in contrast to the previous case, the original DGM element H–56–8 retains some of its advantage over the standard element Q_3 even in subdomain Ω_{f_2} where the evanescent waves appear. The DGM element H–56–8* which contains the enrichment by evanescent wave functions re-establishes the complete performance superiority over the cubic element Q_3 in subdomain Ω_{f_2}, almost to the same level achieved in subdomain Ω_{f_1}. For this higher frequency problem, the performance gain delivered by the further enriched DGM element H–56–8* over the original DGM element H–56–8 is however a little smaller than that delivered in the lower frequency case considered previously. This suggests that at higher frequencies, enriching the approximation by more than eight evanescent wave functionss may be beneficial.

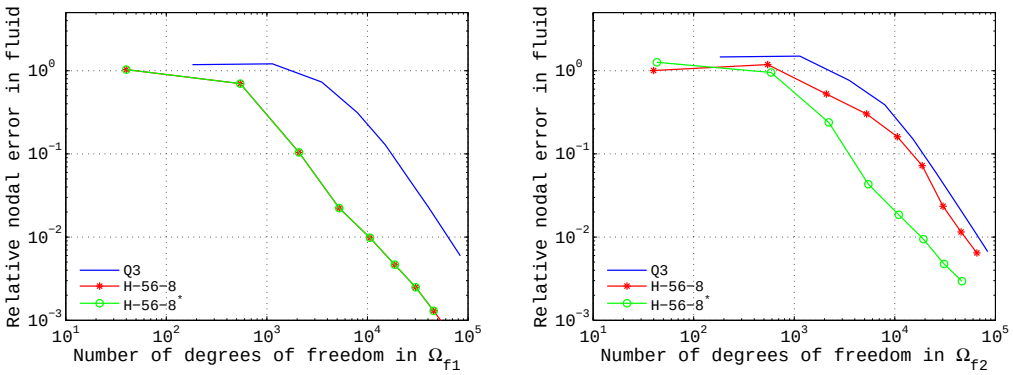

Figure 9. Fluid-fluid wave propagation model problem: comparison of the performances of the elements H–56–8*, H–56–8, and Q_3 for $k_1 = 90$, $k_2 = 20.14$ and $\theta_{inc} = 25^\circ$.

4.2. Elastodynamic evanescent waves

Here, the problem of interest is governed by the boundary value problem (3-9) and defined in the domain $\Omega = [0,1] \times [0,0.25] \times [0,0.5]$. The upper-half subdomain Ω_f is assumed to be filled with water, and the lower-half subdomain Ω_s is assumed to be made of a steel characterized by the Lamé constants $\lambda_L = 9.24e+10$ and $\mu_L = 7.87e+10$. The Robin boundary condition (9) is imposed on the boundary Γ_f with $g_f = \dfrac{\partial p^{\text{ex}}}{\partial \underline{n}} - ikp^{\text{ex}}$, where $p^{\text{ex}} = p_{\text{inc}} + p_r$ is the exact pressure solution in Ω_f. The natural boundary condition (8) with $\underline{g}_s = \underline{\underline{\sigma}}(\underline{u}^{\text{ex}})\underline{n}$ is imposed on the boundary Γ_s, where the exact solution for the displacement field in Ω_s is $\underline{u}^{\text{ex}} = \underline{u}_p + \underline{u}_s$ and is shown in Figure 4. The incident wave p_{inc}, the reflected wave p_r, and the transmitted waves $\underline{u}_p$ and $\underline{u}_s$ are given in Eqs. (54-60).

For this problem, the critical angles for the pressure and shear waves are

$$\theta_{\text{cs}} = 61.87^\circ, \qquad \theta_{\text{cp}} = 74.66^\circ, \tag{70}$$

an evanescent wave can occur only in the solid subdomain, and the parameter θ^{EW} is set in all DGM elements enriched with evanescent wave functions to

$$\theta^{EW} = \frac{1}{2}\theta_{\text{cs}} = 30.94^\circ.$$

As in the case of the fluid-fluid wave propagation model problem, two different uniform mesh scenarios are considered: one with matching size meshes, and one with coarse-fine meshes (Figure 7). In the latter case, the mesh for the solid subdomain is twice coarser than that for the fluid subdomain. The evanescent wave degrees of freedom are activated in subdomain Ω_s only, in the two layers of elements closest to the fluid-solid interface. The discretization error is measured separately in the fluid and solid subdomains Ω_f and Ω_s. In Ω_f, the relative errors are computed using Eqs. (67-68). In Ω_s, they are computed in a similar fashion.

First, the altitude angle of the incident wave is set to $\theta_{\text{inc}} = 25^\circ$. From Eqs. (70), it follows that $\theta_{\text{inc}} < \theta_{\text{cs}} < \theta_{\text{cp}}$. Therefore, the exact solution in the solid subdomain is in this case a combination of an evanescent pressure wave and an evanescent shear wave.

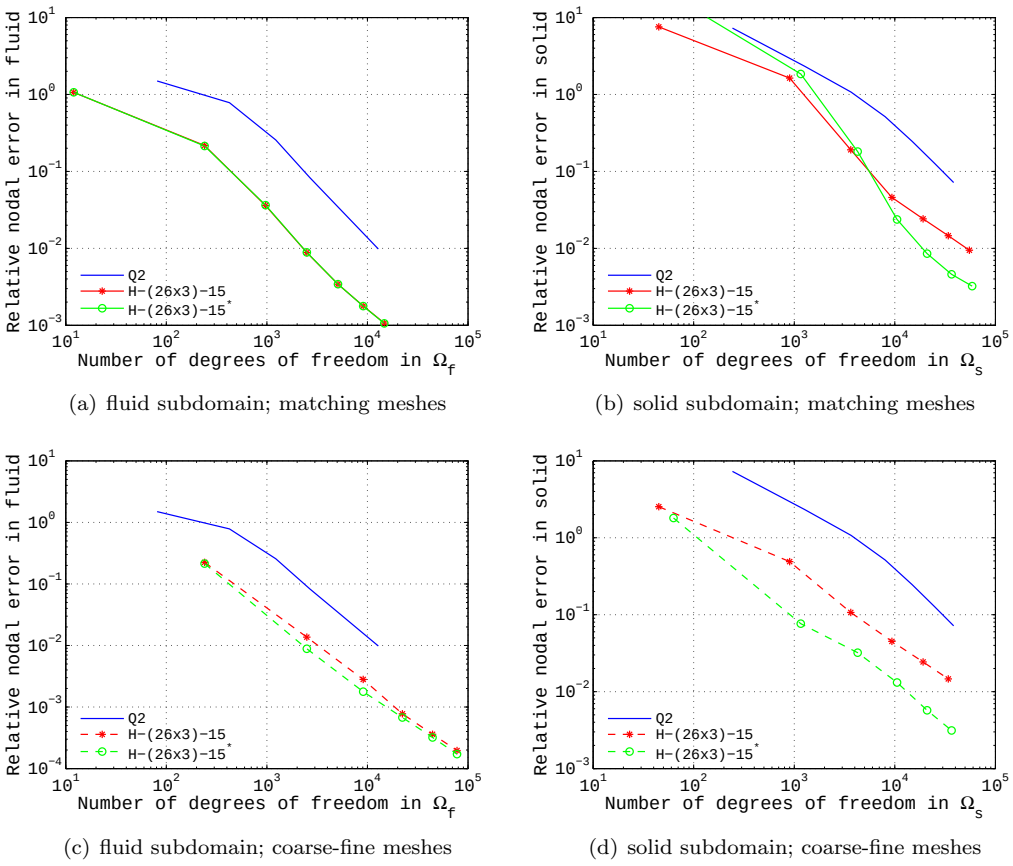

(a) fluid subdomain; matching meshes

(b) solid subdomain; matching meshes

(c) fluid subdomain; coarse-fine meshes

(d) solid subdomain; coarse-fine meshes

Figure 10. Fluid-solid wave propagation model problem: comparison of the performances of the elements H–(26×3)–15, H–(26×3)–15*, and Q_2 for $k = 40$, $k_s = 18.85$, $k_p = 10.58$, and $\theta_{inc} = 25°$.

Figure 10 reports the results obtained for the DGM elements H–(26×3)–15* and H–(26×3)–15, and for the standard Galerkin element Q_2 in the medium frequency regime defined by $k = 40$, $k_p = 10.58$ and $k_s = 18.86$. The DGM element H–(26×3)–15* which is further enriched with evanescent wave functions is found to improve the accuracy achievable by the DGM element H–(26×3)–15 in both meshing scenarios. For the coarse-fine meshes scenario, this improvement is achieved even in the fluid subdomain where no evanescent wave appears, but where the effect of this wave is inherited from the solid subdomain via the fluid-solid interaction. Even when introducing up to 50,000 degrees of freedom, the solution of this problem by the Q_2 element fails to reach a level of relative error as low as 1% in the solid subdomain. On the other hand, the DGM element H–(26×3)–15* delivers this level of accuracy in Ω_s with 10,000 degrees of freedom only. When the target relative error is relaxed to 10% in order to accommodate the performance of the element Q_2 for this problem, the DGM element H–(26×3)–15* achieves this objective in both the solid subdomain using about 40 times fewer

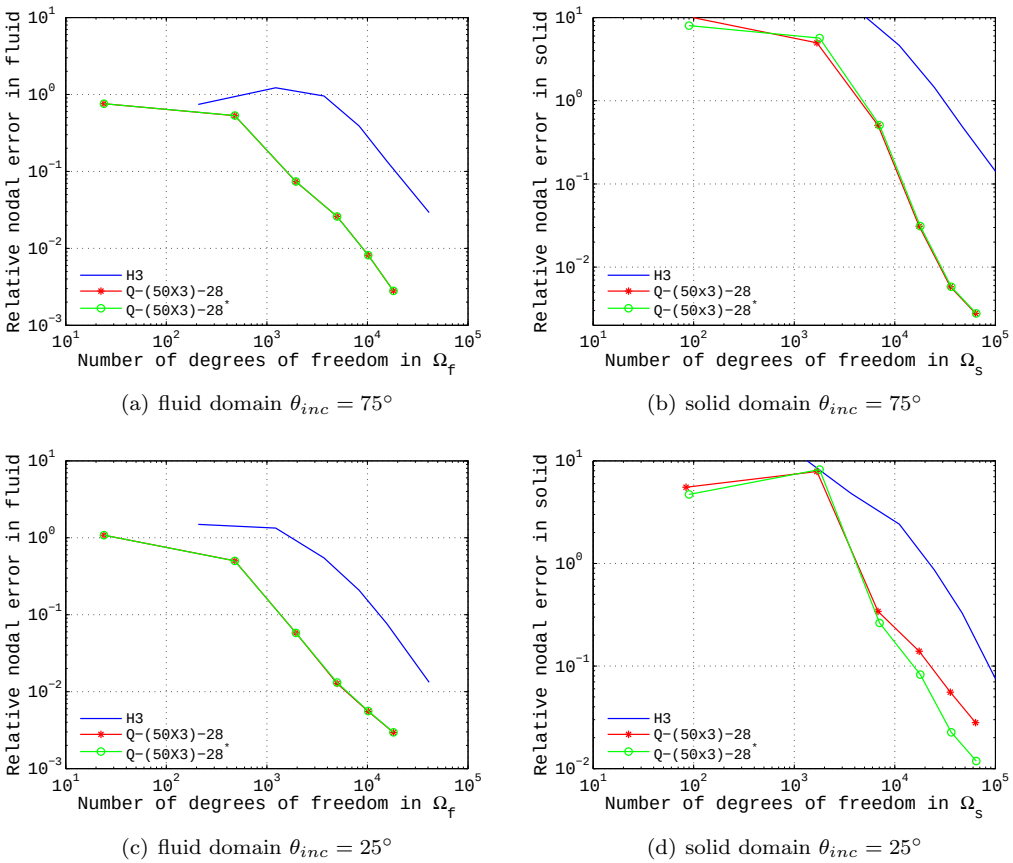

(a) fluid domain $\theta_{inc} = 75°$ (b) solid domain $\theta_{inc} = 75°$

(c) fluid domain $\theta_{inc} = 25°$ (d) solid domain $\theta_{inc} = 25°$

Figure 11. Fluid-solid model wave propagation problem: comparison of H–50×3–28, H–(50×3)–28* and Q_3 for $k = 80$, $k_s = 37.71$, $k_p = 21.15$.

degrees of freedom than Q_2.

Next, the frequency is increased so that the wave numbers become $k = 80$, $k_p = 21.15$, and $k_s = 37.71$. The higher-order elements H–(50×3)–28*, H–(50×3)–28, and Q_3 are then considered for the solution of the following fluid-solid interaction problems. First, θ_{inc} is set to $\theta_{inc} = 75°$ so that no evanescent wave is produced in either subdomain. Figure 11 (a-b) shows that in this case, both considered DGM elements yield virtually the same performance results and outperfom the cubic element Q_3 by more than one order of magnitude in the subdomain Ω_s, while exhibiting approximately the same rate of convergence. Next, θ_{inc} is set to $\theta_{inc} = 25°$ so that two pressure and shear evanescent waves are created in the solid subdomain. In this case, the performance results displayed in Figure 11 (c-d) show that the asymptotic convergence rate of the DGM element H–(50×3)–28 is improved when evanescent wave functions are added to its set of enrichment functions. In the solid subdomain, the discretization by the DGM element H–(50×3)–28* is found to reach the 90% level of accuracy using approximately seven

times fewer degrees of freedom than that by the standard cubic Galerkin element Q_3.

5. CONCLUSION

Evanescent waves occur in multi-material media when the altitude angle of an incident wave is below a critical value. When the different media are characterized by sufficiently different speeds of sound, these small-scale waves transform a wave propagation problem into a genuine multiscale problem that is difficult to solve numerically by standard approximation methods. Enrichment-based discretization approaches such as the Discontinuous Enrichment Method (DEM) and its variant known as the Discontinuous Galerkin Method (DGM) with Lagrange multipliers can be well-suited for solving such problems, if appropriate enrichment fields are chosen. In this paper, it is shown that whereas plane wave shape functions can efficiently capture acoustic scattering fields in the absence of evanescent waves, including in the medium frequency regime, they sometimes do not perform significantly better than higher-order polynomial approximations in the presence of such waves. On the other hand, further enrichment of plane wave based elements with evanescent wave shape functions is shown to lead to high-performance multiscale elements that effectively capture all of the reflected and transmitted waves in a multi-material problem. Numerical tests performed in three-dimensions for various fluid-fluid and fluid-solid wave propagation model problems reveal that DGM elements with Lagrange multipliers combining plane wave and evanescent wave shape functions can reduce the number of degrees of freedom required by either the DGM elements with plane wave shape functions only, or the standard higher-order polynomial finite elements, by up to a factor larger than a full order of magnitude.

Acknowledgments

The authors acknowledge the support by the Office of Naval Research under Grant N00014-05-1-0204-1.

REFERENCES

1. C. Farhat, I. Harari and L.P. Franca. The discontinuous enrichment method. *Comput. Methods Appl. Mech. Engrg.*, **190**:6455–6479, 2001.
2. C. Farhat, I. Harari and U. Hetmaniuk. A discontinuous Galerkin method with Lagrange multipliers for the solution of Helmholtz problems in the mid-frequency regime. *Comput. Methods Appl. Mech. Engrg.*, **192**:1389–1419, 2003.
3. C. Farhat, I. Harari and U. Hetmaniuk. The discontinuous enrichment method for multiscale analysis. *Comput. Methods Appl. Mech. Engrg.*, **192**:3195–3210, 2003.
4. C. Farhat, R. Tezaur and P. Weidemann-Goiran. Higher-order extensions of a discontinuous Galerkin method for mid-frequency Helmholtz problems. *Int. J. Numer. Meth. Engng.*, **61**:1938–1956, 2004.
5. C. Farhat, P. Wiedemann-Goiran and R. Tezaur. A discontinuous Galerkin method with plane waves and Lagrange multipliers for the solution of short wave exterior Helmholtz problems on unstructured meshes. New computational methods for wave propagation. *Wave Motion*, **39**(4):307–317, 2004.
6. L. Zhang, R. Tezaur and C. Farhat. The discontinuous enrichment method for elastic wave propagation in the medium-frequency regime. *Int. J. Numer. Meth. Engng.*, **66**:2086–2114, 2006.

7. R. Tezaur and C. Farhat. Three-dimensional discontinuous Galerkin elements with plane waves and Lagrange multipliers for the solution of mid-frequency Helmholtz problems. *Int. J. Numer. Meth. Engng.*, **66**:796–815, 2006.
8. R. Tezaur, L. Zhang, and C. Farhat. A discontinuous enrichment method for capturing evanescent waves in multi-scale fluid and fluid/solid problems. *Comput. Methods Appl. Mech. Engrg.*, in print, 2007.
9. K.F. Graff. *Wave Motion in Elastic Solids*. Dover, New York, 1991.
10. J.A. DeSanto. *Scalar Wave Theory*. Springer-Verlag, 1992.
11. F. Ihlenburg. *Finite Element Analysis of Acoustic Scattering*. Springer, 1998.
12. J. Billingham and A.C. King. *Wave Motion*. Cambridge University Press, 2000.
13. T. Hunt. What Everyone Needs to Know About Evanescent Fields. *http://www.physics.harvard.edu/ tomhunt/pubs/evanescent.pdf*, 2003.
14. F. Fornel. *Evanescent Waves: From Newtonian Optics to Atomic Optics*. Springer, 2002.
15. L.L Thompson, S. Sankar and Y. Tong. Complex wave-number dispersion analysis of stabilized finite element methods for acoustic fluid - structure interaction. *Proceedings of SECTAM-XX*, :1–9, 2000. April 16-18, Callaway Gardens, GA.
16. G. Barbastathis. Optics Course Notes. *http://web.mit.edu/2.710/www/*, 2002.
17. M.K. Hong, A. Swan and S. Erramilli. Evanescent wave vibrational microscopy. *Optics & Photonics News*, (July):30–35, 2004.
18. *http://www.mtronpti.com*.
19. H.J. Simpson and B.H. Houston. Laboratory measurements of sound scattering from a buried sphere above and below the critical angle. *J. Acoust. Soc. Am.*, **113**(1):39–42, 2003.
20. J. M. Melenk. *On Generalized Finite Element Methods*. Ph.D. Thesis, University of Maryland, College Park, MD, 1995.
21. T. Strouboulis, K. Copps and I. Babuška. The generalized fintie element method. *Comput. Methods Appl. Mech. Engrg.*, **190**:4081–4193, 2001.
22. T. Strouboulis, L. Zhang and I. Babuška. p-version of the Generalized FEM using mesh-based handbooks with applications to multiscale problems. *Int. J. Numer. Meth. Engng.*, **60**:1639–1672, 2004.
23. E. Vitali and D.J. Benson. An extended finite element formulation for contact in multi-material arbitrary Lagrangian-Eulerian calculations. *Int. J. Numer. Meth. Engng.*, **67**:1420–1444, 2006.
24. C. Daux, N. Moës, J. Dolbow, N. Sukumar and T. Belytschko. Arbitrary branched and intersecting cracks with the extended finite element method. *Int. J. Numer. Meth. Engng.*, **48**:1741–1760, 2000.
25. T. Belytschko, C. Parimi, N. Moës, N. Sukumar, and S. Usui. Structured extended finite element methods for solid defined by implicit surfaces. *Int. J. Numer. Meth. Engng.*, **56**:609–635, 2003.
26. G. Ventura. On the elimination of quadrature subcells for discontinuous functions in the extended finite element method. *Int. J. Numer. Meth. Engng.*, **66**:761–795, 2006.
27. R. Gracie, G. Ventura, and T. Belytschko. A new fast finite element method for dislocations based on interior discontinuities. *Int. J. Numer. Meth. Engng.*, **69**:423–441, 2007.
28. C.A. Duarte and J.T. Oden. An hp adaptive method using clouds. *Comput. Methods Appl. Mech. Engrg.*, **139**:237–262, 1996.
29. J. T. Oden, C. A. Duarte, and O. C. Zienkiewicz. A new cloud-based hp finite element method. *Comput. Methods Appl. Mech. Engrg.*, **153**:117–126, 1998.
30. P. Monk and D.Q. Wang. A least-squares method for the Helmholtz equation. *Comput. Methods Appl. Mech. Engrg.*, **175**:121–136, 1999.
31. T. Huttunen, P. Monk, F. Collino and J.P. Kaipio. The ultra-weak variational formulation for elastic wave problems. *SIAM J. Sci. Comp.*, **25**(5):1717–1742, 2004.
32. P. Ladevèze and H. Riou. Calculation of medium-frequency vibrations over a wide frequency range. *Comput. Methods Appl. Mech. Engrg.*, **194**:3167-3191, 2005.
33. R.A. Adams. *Sobolev Spaces*. Academic Press, New York, 1975.